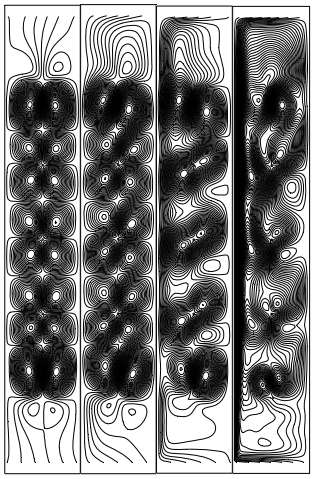

Fig. 5.31 Stream function contours of uniform arrangement (V_0 = 17.5 kV and N = 5) (a) Ra = 10^4, (b) Ra = 10^5, (c) Ra = 10^6, (d) Ra = 10^7.

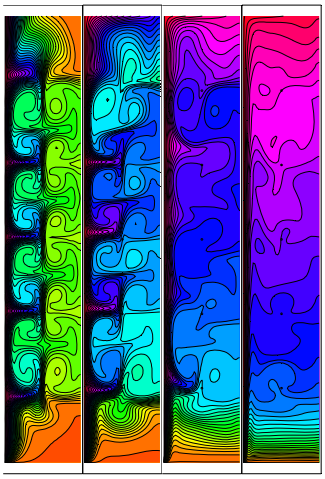

Fig. 5.32 Temperature distributions of uniform arrangement (V_0 = 17.5 kV and N = 5) (a) Ra = 10^4, (b) Ra = 10^5, (c) Ra = 10^6, (d) Ra = 10^7.

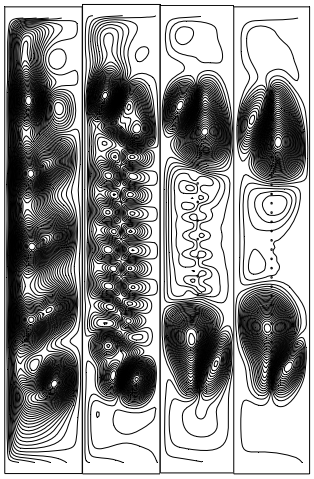

(a) (b) (c) (d)

Fig. 5.33 Stream function contours of unequal number of electrodes (V_0 = 17.5 kV and Ra = 10^6) (a) N = 5, (b) N = 9, (c) N = 17, (d) N = 33.

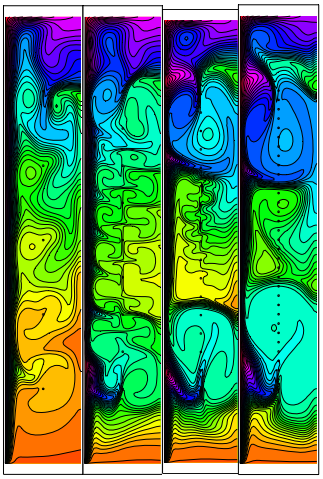

(a) (b) (c) (d)

Fig. 5.34 Temperature distributions of unequal number of electrodes (V_0 = 17.5 kV and Ra = 10^6) (a) N = 5, (b) N = 9, (c) N = 17, (d) N = 33.

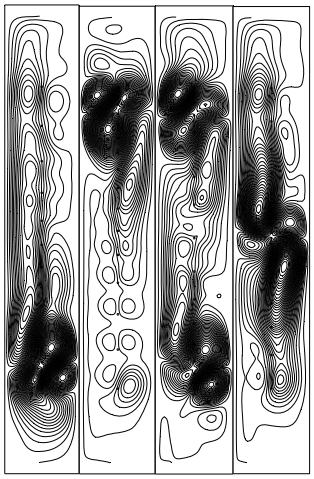

(a) (b) (c) (d)

Fig. 5.35 Stream function contours of various electrode arrangements (V_0 = 17.5 kV, Ra = 10^6, and N = 17) (a) bottom denseness, (b) top denseness, (c) ends denseness, (d) middle denseness.

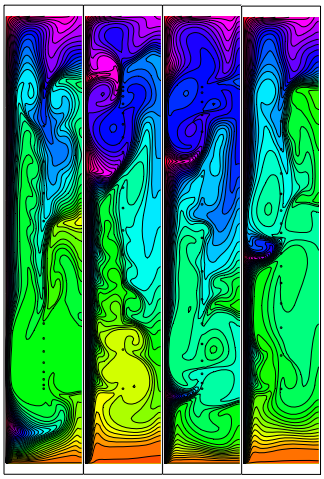

(a) (b) (c) (d)

Fig. 5.36 Temperature distributions of various electrode arrangements (V_0 = 17.5 kV, Ra = 10^6, and N = 17) (a) bottom denseness, (b) top denseness, (c) ends denseness, (d) middle denseness.

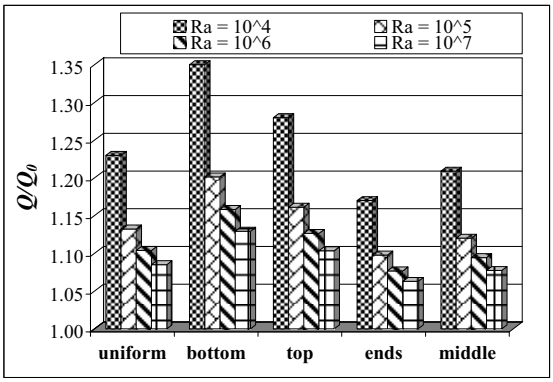

Fig. 5.37 Electrode arrangement effect to the volume flow rate (V_0 = 17.5 kV and N = 17).

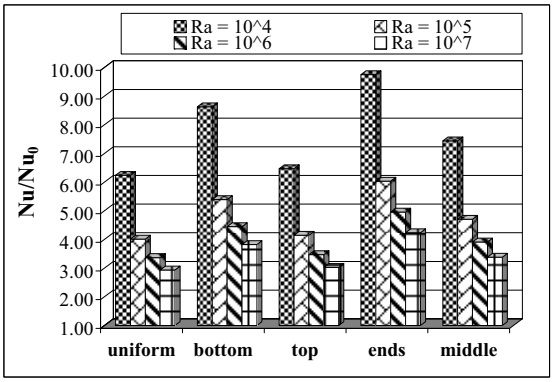

Fig. 5.38 Electrode arrangement effect to the heat transfer (V_0 = 17.5 kV and N = 17).

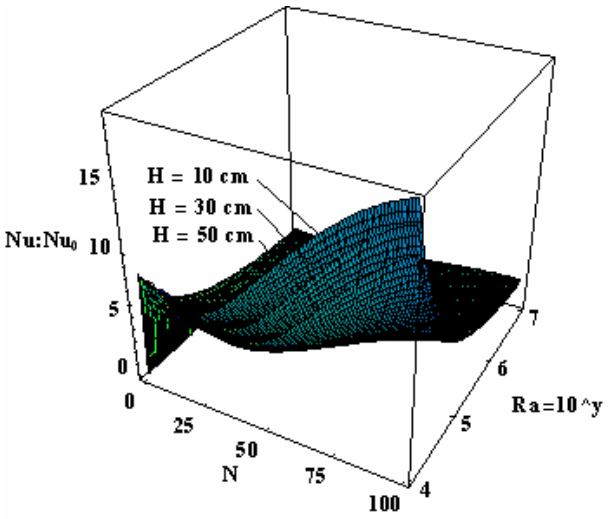

Fig. 5.39 Augmented ratio in relation with aspect ratio (V_0 = 17.5 kV and W = 5 cm).

Fig. 5.40 conducts the flow and temperature fields of four different electrode positions; (x = 3.5 cm, y is between the fins), (x = 3.5 cm, y is on the fin strip), (x = 2.5 cm, y is between the fins), and (x = 1.0 cm, y is between the fins) when the numbers of fins and electrodes are also kept at seven (V_0 = 12.0 kV, Ra = 10^6, N_f = 7, N_e = 7, L_f = 0.4, and ϕ = 90°). It can be observed that the third arrangement (Fig. 5.40(c)) performs a maximum volume flow rate from a highest velocity along a hot wall compared with other arrangement due to the circulation below the fins is relatively stronger and more complete, as a result of which the flow around the fins is with a vortex formed on the fins, while the last arrangement (Fig. 5.40(d)) yields the pair of vortices which reduces the flow structure from a high intensity of electric field.

The oscillatory stream function and isotherm line contours for various numbers of electrodes as 1, 3, 13, and 26 are expressed in Fig. 5.41 (V_0 = 12.0 kV, Ra = 10^6, N_f = 7, L_f = 0.4, and ϕ = 90°). Effect of the number of electrodes plays much important role on the flow pattern of air inside a vertical channel. It can be observed that the number of vortices increases when the number of electrodes is augmenting from 1 to 13, but the vortices are combining when the number of electrodes reaches a sufficient value in Fig. 5.41(d) which the large vortices occur especially around the extremes of an electrode strip. The isotherm lines show a formation of the boundary layer heat transfer along a hot wall. As seen that temperature gradient at a hot wall of Fig. 5.41(c) has a highest value, it means that this categories also achieves a maximum heat transfer coefficient. Therefore, it can be concluded that the number of electrodes has more significant at an optimum value. However, it should be compared between the extra received heat transfer and power of electrical energy input for an optimized design.

A non-equivalent number of fins dominates the different flow patterns to occur in the channels of Fig. 5.42 (V_0 = 12.0 kV, Ra = 10^6, N_e = 7, L_f = 0.4, and ϕ = 90°): (a) N_f = 1, (b) N_f = 3, (c) N_f = 5, and (d) N_f = 13. Temperature contours along the channel of Fig. 5.42(a) is quite similarly with the case of no fin attached from the less remarkable effect by a single fin. The separation points over the fins are enhanced accordingly with the number of fins. In Fig. 5.43 (V_0 = 12.0 kV, Ra = 10^6, N_f = 7, N_e = 7, and ϕ = 90°): (a) L_f = 0.1, (b) L_f = 0.2, (c) L_f = 0.6, and (d) L_f = 0.8, a character of the clockwise and counter-clockwise rotating vortices is unaltered, with longer fins bringing about more change to the flow compared with shorter fins. For shorter fins, almost all positions only change the temperature distribution locally and the rest of a hot wall remains unaffected. This is

because the primary flow cannot alter too much upon introduction of a short length and the fins only change the velocity distribution locally. It is noticed that for $L_f > 0.5$ (Fig. 5.43(c) and (d)), many recirculating vortices are found above the fins and a long length has more remarkable effects on the flow field.

In Fig. 5.44 (V_0 = 12.0 kV, N_f = 7, N_e = 7, L_f = 0.4, and ϕ = 90°), the electrode arrangement in Fig. 5.40(c) becomes a most remarkable effect with a rising of the convective heat transfer rate due to the fact that it has a minimum thermal boundary layer thickness along a channel. Fig. 5.45 demonstrates relation between the heat transfer and number of electrodes (V_0 = 12.0 kV, N_f = 7, L_f = 0.4, and ϕ = 90°). Nusselt number varies accordingly with respect to the number of electrodes. The trend of curve also reaches a maximum point at an intermediate number and becomes rising again when the number of electrode is rather high from the high intensity of electric field. This phenomenon can be analyzed by considering the isotherm line density in Fig. 5.41(c) at N = 13 which found to be higher than at N = 1 (Fig. 5.41(a)) due to lower heat trap that causes higher heat transfer coefficient. Since the number of electrodes is rather high as N = 26, many vortices are formulated along the channel and combined even though there is a good turbulent mixing, but the flows are recirculating and oscillating especially around the top and bottom zones. Surprisingly, at a high number of electrodes, the Nusselt number is slightly tapered off that is not occurred in the case for no fin attached, the reason for which follows the observation made in Fig. 5.41 regarding the effect of number of fins and fin length that will be discussed later.

Fig. 5.46 conduct relation between the heat transfer with the number of fins at the same fin length (N_e = 7, L_f = 0.4, and ϕ = 90°). The Nusselt number decreases monotonously with the number of fins due to a low convective heat transfer that occurred at a high number of fins. The effect of fin length on the electrohydrodynamic enhanced heat transfer is conducted in Fig. 5.47 (N_f = 7, N_e = 7, and ϕ = 90°). Nusselt number is also a decreasing function of the fin length because it is dominated by the conduction at a long fin length but which is considerably improved by the electric field when explaining in term of the ratio between EHD per non-EHD.

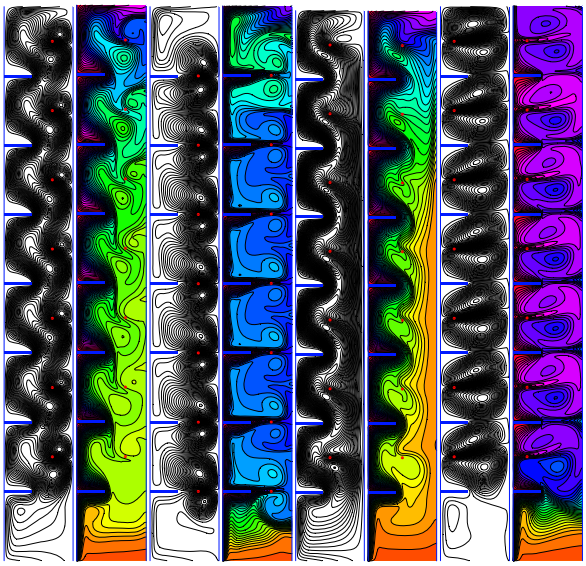

(a) (b) (c) (d)

Fig. 5.40 Effect of the electrode arrangement on the flow and temperature fields (V_0 = 12.0 kV, Ra = 10^6, N_f = 7, N_e = 7, L_f = 0.4, and ϕ = 90°): (a) x = 3.5 cm, y is between the fins, $\Delta\bar{\psi} = 2.0 \times 10^{-4}$, $\Delta\theta = 2.5 \times 10^{-2}$, (b) x = 3.5 cm, y is on the fin strip, $\Delta\bar{\psi} = 2.0 \times 10^{-4}$, $\Delta\theta = 2.5 \times 10^{-2}$, (c) x = 2.5 cm, y is between the fins, $\Delta\bar{\psi} = 2.0 \times 10^{-4}$, $\Delta\theta = 2.5 \times 10^{-2}$, and (d) x = 1.0 cm, y is between the fins, $\Delta\bar{\psi} = 2.0 \times 10^{-4}$, $\Delta\theta = 2.5 \times 10^{-2}$.

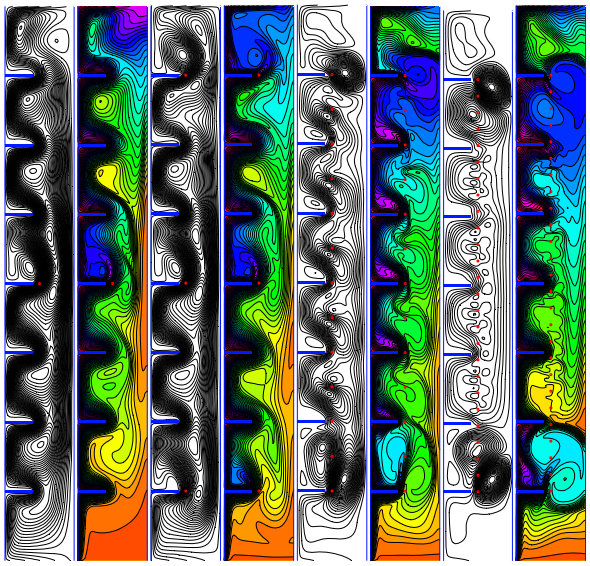

(a) (b) (c) (d)

Fig. 5.41 Number of electrodes effect on the flow and temperature fields inside the finned vertical channels (V_0 = 12.0 kV, Ra = 10^6, N_f = 7, L_f = 0.4, and ϕ = 90°): (a) N_e = 1, $\Delta\bar{\psi}$ = 1.5×10^{-4}, $\Delta\theta$ = 2.5×10^{-2}, (b) N_e = 3, $\Delta\bar{\psi}$ = 1.7×10^{-4}, $\Delta\theta$ = 2.5×10^{-2}, (c) N_e = 13, $\Delta\bar{\psi}$ = 2.2×10^{-4}, $\Delta\theta$ = 2.5×10^{-2}, and (d) N_e = 26, $\Delta\bar{\psi}$ = 2.8×10^{-4}, $\Delta\theta$ = 2.5×10^{-2}.

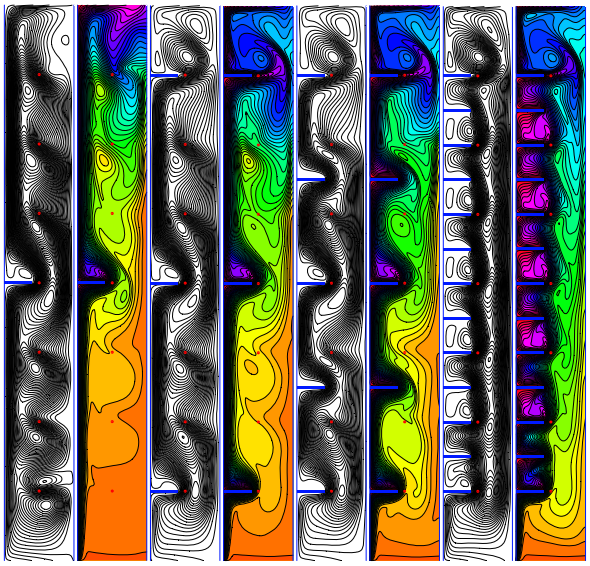

(a) (b) (c) (d)

Fig. 5.42 Number of fins effect on the flow and temperature fields inside the finned vertical channels (V_0 = 12.0 kV, Ra = 10^6, N_e = 7, L_f = 0.4, and ϕ = 90°): (a) N_f = 1, $\Delta\bar{\psi}$ = 2.0×10^{-4}, $\Delta\theta$ = 2.5×10^{-2}, (b) N_f = 3, $\Delta\bar{\psi}$ = 2.0×10^{-4}, $\Delta\theta$ = 2.5×10^{-2}, (c) N_f = 5, $\Delta\bar{\psi}$ = 2.0×10^{-4}, $\Delta\theta$ = 2.5×10^{-2}, and (d) N_f = 13, $\Delta\bar{\psi}$ = 2.0×10^{-4}, $\Delta\theta$ = 2.5×10^{-2}.

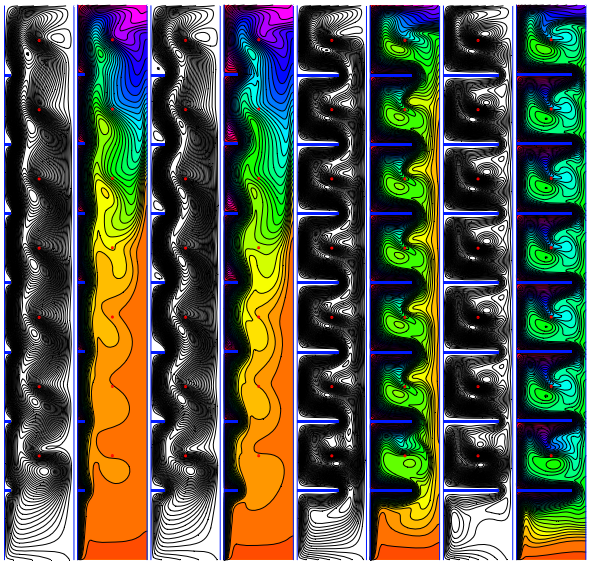

(a) (b) (c) (d)

Fig. 5.43 Stream function and isotherm line contours inside the finned vertical channels for various fin lengths (V_0 = 12.0 kV, Ra = 10^6, N_f = 7, N_e = 7, and ϕ = 90°): (a) L_f = 0.1, $\Delta\bar{\psi}$ = 2.0×10^{-4}, $\Delta\theta$ = 2.5×10^{-2}, (b) L_f = 0.2, $\Delta\bar{\psi}$ = 2.0×10^{-4}, $\Delta\theta$ = 2.5×10^{-2}, (c) L_f = 0.6, $\Delta\bar{\psi}$ = 2.0×10^{-4}, $\Delta\theta$ = 2.5×10^{-2}, and (d) L_f = 0.8, $\Delta\bar{\psi}$ = 2.0×10^{-4}, $\Delta\theta$ = 2.5×10^{-2}.

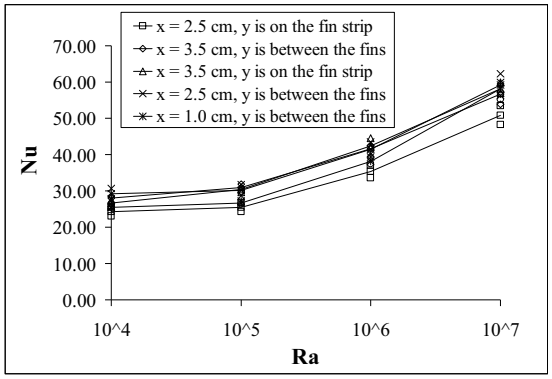

Fig. 5.44 Effect of the electrode arrangements on the heat transfer (V_0 = 12.0 kV, N_f = 7, N_e = 7, L_f = 0.4, and ϕ = 90°).

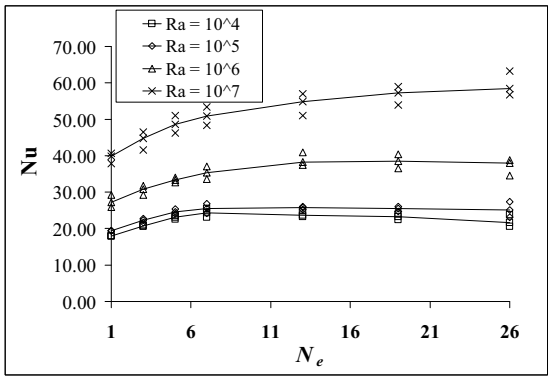

Fig. 5.45 Nusselt number for various number of electrodes (V_0 = 12.0 kV, N_f = 7, L_f = 0.4, and ϕ = 90°).

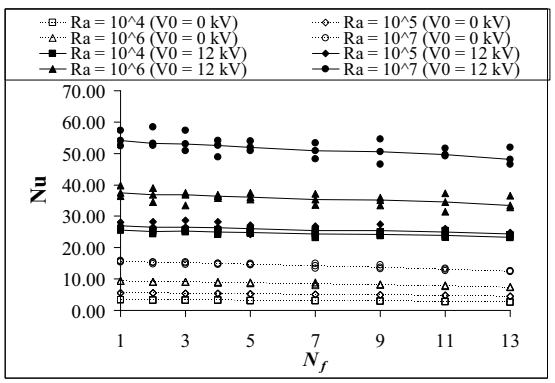

Fig. 5.46 Number of fins effect on the Nusselt number (N_e = 7, L_f = 0.4, and ϕ = 90°).

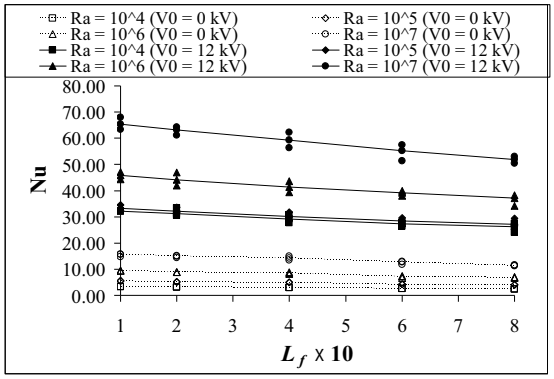

Fig. 5.47 Nusselt number at each fin length ($N_f = 7$, $N_e = 7$, and $\phi = 90°$).

5.4 Open Cavity Configuration

Fig. 5.48 investigates the computational domain and concerning boundary conditions of partially open square cavities. The left plate is maintained at uniform temperature and the right opening is also kept at uniform temperature of 300 K. Left plate is electrically grounded and upper, lower, and right plates are thermally and electrically insulated. The dimension of an open square cavity is 15 × 15 cm^2. To validate the numerical code, the numerical results of non-EHD effect are validated against with the benchmark numerical solutions of the horizontal open square cavity with an extended computational domain. It is found that the highest percentage difference of the Nusselt numbers is 4.6% for Ra =10^4 and the lowest is 0.3% for Ra =10^7. Fig. 5.49 investigates the stream function and isotherm lines contours from applying the EHD effect while the Rayleigh numbers is varied between 10^4 to 10^7, in which the effect of Joule heating at the wire electrode is neglected (V_0 = 15.0 kV, N = 3, $\theta = 90°$, AR = 0.5, and AH = 0.5). There is an effect of the secondary flow induced by the ionic wind at the wire electrodes, which causes four rotating cellular motions in Fig. 5.49(a). In next cases, where the Rayleigh number is increased further, the fluid inside cavity is dominated by the effect of Rayleigh number instead of an electric field. The flow patterns are oscillatory due to the interaction between the thermal buoyancy force and electrical body force. Two categories of oscillations are observed in these figures; periodic state (Figs. 5.49(a)-(b)) and non periodic state (Figs. 5.49(c)-(d)). The thermal boundary layer is perturbed by the electric field when it extends over the recirculation region. It can be seen that temperature gradient (line density) at the left plate

becomes larger with an increasing of Rayleigh number, which causes high heat transfer coefficient. It can be concluded that for low Rayleigh number, the flow and temperature fields have been substantially affected due to an electric field. However, the effect of EHD is diminished at high Rayleigh number which can be indicated that no significantly change in the heat transfer enhancement.

Fig. 5.50 performs the effect of aperture size and aperture position to flow pattern and temperature distribution in the open square cavities with (a) AR = 0.5, AH = 0.25, (b) AR = 0.5, AH = 0.75, (c) AR = 0.75, AH = 0.5, and (d) AR = 0.25, AH = 0.5 (V_0 = 15.0 kV, Ra = 10^6, N = 3, and θ = 90°). The effect of the aperture position is presented in Figs. 5.50(a) and (b) (AR = 0.5) for AH = 0.25 and 0.75, respectively. In Fig. 5.50(a), the air enters the cavity at the lower part paralleled to the lower wall, heated up at the hot wall and moves up to the top, and exit at the upper part of the opening, which similarly in Fig. 5.50(b) but the flow strength is weakness than the first case. Thus, at low aperture position, the convection is highest, as a result of which heat transfer should be better. The effect of aperture size is shown in Figs. 5.50(c) and (d) for AR = 0.75 and 0.25, respectively. It can be seen that convection is enhanced with larger aperture.

The effect for various numbers of electrodes from 5, 9, 17, and 28 are expressed in Fig. 5.51 (V_0 = 15.0 kV, Ra = 10^6, θ = 90°, AR = 0.5, and AH = 0.25), in which the lower aperture position is selected for this study due to the highest volume flow rate and also heat transfer coefficient from Fig. 5.50. A non-equivalent number of electrodes cause different flow patterns to occur in the cavity. It can be observed that the separation point at the left plate appears when the number of electrodes is augmented to 9. The large vortices occur at the upper and lower of the cavities of Figs. 5.51(c)-(d), especially around the electrode strip that divides recirculating cells in three zones. As seen that temperature gradient along the left plate of Fig. 5.51(b) is highest compared with other categories that may results in maximum heat transfer coefficient. Moreover, the extra received heat transfer is very larger compared with the power input of electrical energy. Fig. 5.52 presents the effect of inclination to the flow pattern and temperature distribution in the open square cavities with θ = 0°, 30°, 60°, and 120° (V_0 = 15.0 kV, Ra = 10^6, N = 3, AR = 0.5, and AH = 0.25). The case for θ = 0° in Fig. 5.52(a) corresponds that a convective regime is developed and the convection strength has strongest at θ = 60° in Fig. 5.52(c). In contrast, when the inclined angle increases further, especially at 120° (Fig. 5.52(d)), the circulation strength is considerably reduced and a non-symmetrical cells occur as same as at θ = 60°. This is

expected since the cold fluid enters the cavities added by the gravity and the hot fluid exits almost horizontally. It can be seen that temperature gradient along the hot plate in case of θ = 60° is highest, thus, convective heat transfer should be highest. At θ = 120°, the isotherms indicate quasi-conductive regime along the boundaries because the hot plate is facing downward on this case.

The average volume flow rate and heat transfer enhancements over the period of periodic state or over the entire time span of non-periodic state along a cavities for various Rayleigh numbers is investigated in Figs. 5.53 and 5.54 (N = 3, θ = 90°, AR = 0.5, and AH = 0.5), respectively. It can be seen that EHD enhancement of flow and heat transfer plays much important role at the low Rayleigh number and high supplied voltage. The number of electrodes also has high effect to the total volume flow rate through the cavity in Fig. 5.55 (V_0 = 15.0 kV, θ = 90°, AR = 0.5, and AH = 0.25). The enhanced volume flow rate ratio increases to a maximum at an intermediate number of electrodes, and decreases at the high number of electrodes due to the raising of pressure drop. Fig. 5.56 demonstrates the relation between heat transfer enhancement and number of electrodes (V_0 = 15.0 kV, θ = 90°, AR = 0.5, and AH = 0.25). Augmented Nusselt number reaches a minimum at an intermediate number of, and increases again due to the high intensity of the electric field at higher number of electrodes. This phenomenon can be analyzed by considering the isotherm line density at the left plate of Fig. 5.51. For the case N = 9, the density is found to be higher than at N = 5 due to lower number of vortices and also the smaller heat trap that yields a higher heat transfer coefficient.

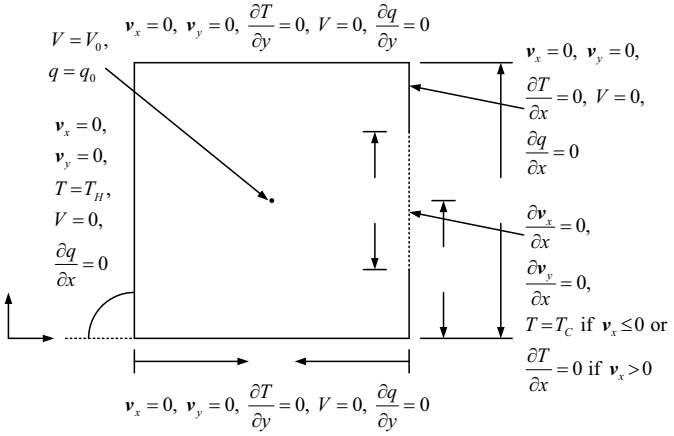

Fig. 5.48 Boundary conditions of the partially open square cavity.

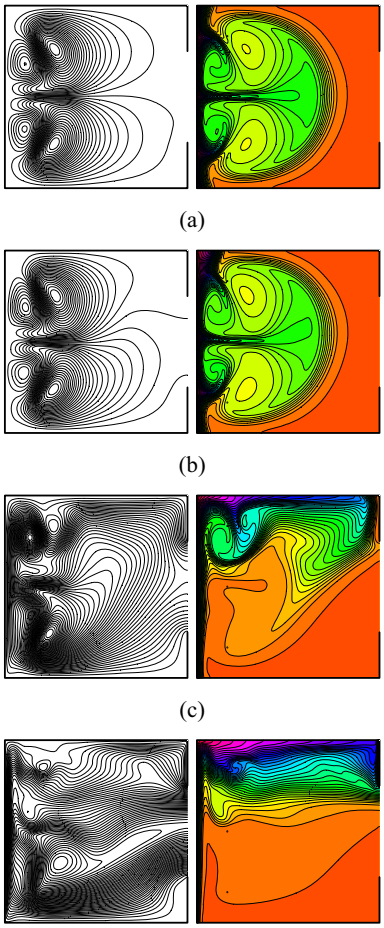

Fig. 5.49 Stream function and isotherm line contours inside the cavities for various Rayleigh numbers (V_0 = 15.0 kV, N = 3, θ = 90°, AR = 0.5, and AH = 0.5): (a) Ra = 10^4, (b) Ra = 10^5, (c) Ra = 10^6, and (d) Ra = 10^7.

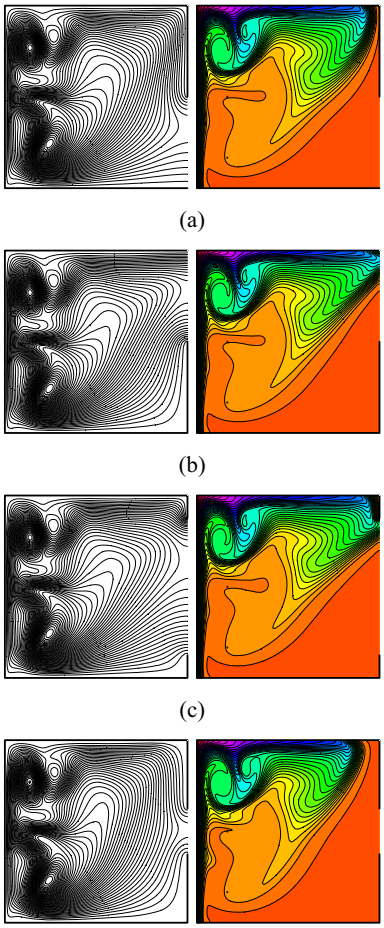

Fig. 5.50 Effect of the aperture size and aperture position to the flow and temperature fields (V_0 = 15.0 kV, Ra = 10^6, N = 3, and θ = 90°): (a) AR = 0.5, AH = 0.25, (b) AR = 0.5, AH = 0.75, (c) AR = 0.75, AH = 0.5, and (d) AR = 0.25, AH = 0.5.

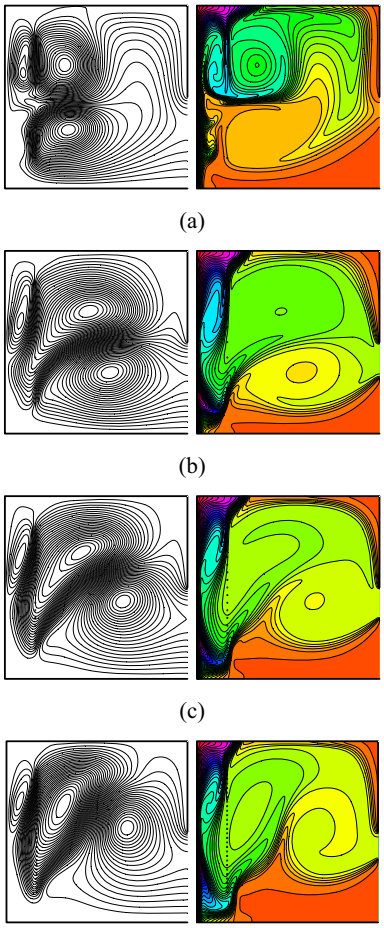

Fig. 5.51 Stream function and isotherm line contours inside the cavities for various numbers of electrodes (V_0 = 15.0 kV, Ra = 10^6, θ = 90°, AR = 0.5, and AH = 0.25): (a) N = 5, (b) N = 9, (c) N = 17, and (d) N = 28.

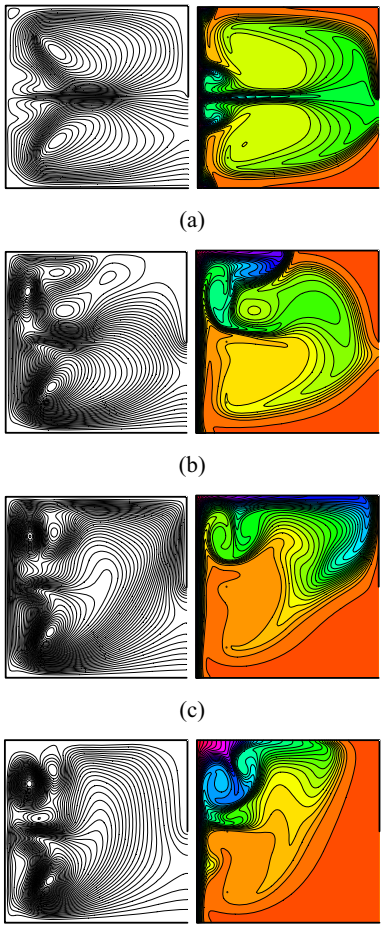

Fig. 5.52 Effect of the inclined angle to the flow and temperature fields (V_0 = 15.0 kV, Ra = 10^6, N = 3, AR = 0.5, and AH = 0.25): (a) θ = 0°, (b) θ = 30°, (c) θ = 60°, and (d) θ = 120°.

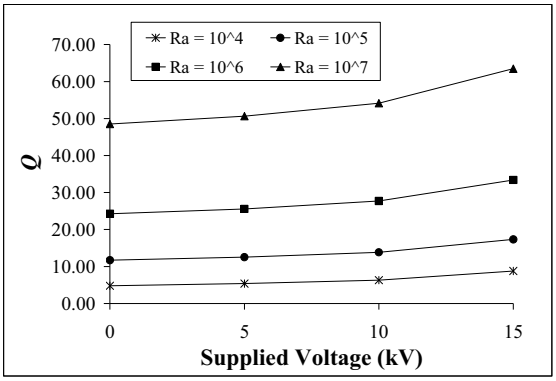

Fig. 5.53 Volume flow rate as a function of the supplied voltage ($N = 3$, $\theta = 90°$, AR = 0.5, and AH = 0.5).

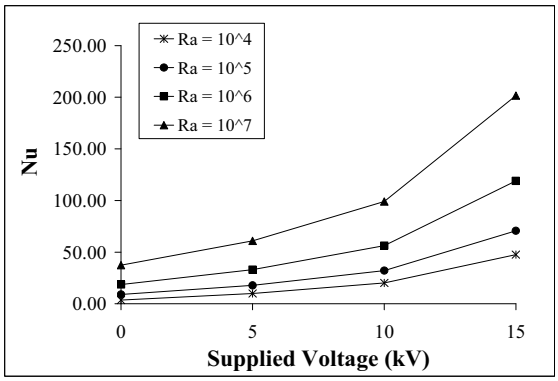

Fig. 5.54 Nusselt number as a function of the supplied voltage ($N = 3$, $\theta = 90°$, AR = 0.5, and AH = 0.5).

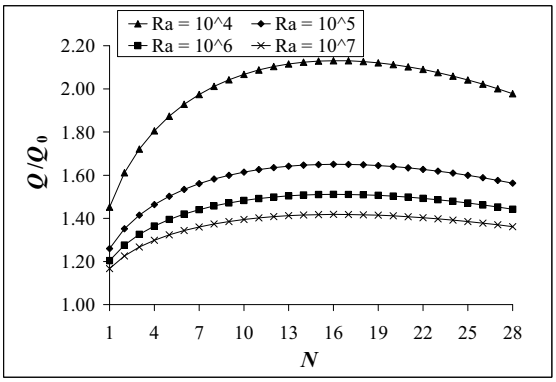

Fig. 5.55 Volume flow rate enhancement as a function of the number of electrodes ($V_0 = 15.0$ kV, $\theta = 90°$, AR = 0.5, and AH = 0.25).

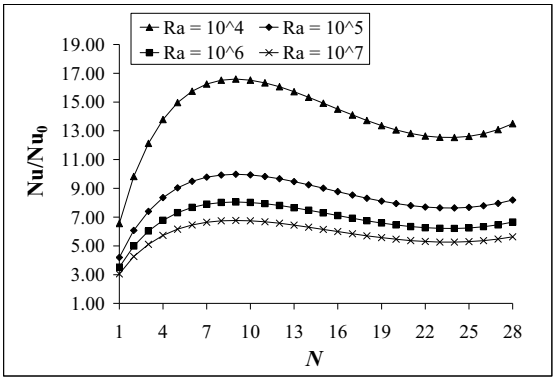

Fig. 5.56 Heat transfer enhancement as a function of the number of electrodes (V_0 = 15.0 kV, θ = 90°, AR = 0.5, and AH = 0.25).

Fig. 5.57 investigates the stream function and isotherm line contours inside the cavities with a thin fin attached at the middle of the left wall and has the length of 0.25 W by applying the EHD effect while the Rayleigh numbers is varied between 10^4 to 10^7, in which the effect of Joule heating at the wire electrode is neglected (V_0 = 12.0 kV, N = 1, θ = 90°, AR = 0.5, and AH = 0.5). For non-EHD, the fluid moves up due to heating on the left wall and consequent exiting on the right opening creates a clockwise-rotating vector. For low Rayleigh number, the strength of the primary vortex is weakened due to the fin obstructs the movement of fluid. This is because the convection not being strong compared with the conduction and it has the most remarkable effects on the flow field when it is placed at the middle of the left wall. It appears that the stream lines become more packed with the increasing of Rayleigh number, thus, the fluid moves faster as natural convection is intensified. For applying EHD (the electrode is positioned at the center of cavity), there is an effect of the secondary flow induced by the ionic wind at the wire electrodes, which causes two rotating cellular motions in Fig. 5.57(a). In next cases, where the Rayleigh number is increased further, the fluid inside cavity is dominated by the effect of Rayleigh number instead of an electric field. The flow patterns are oscillatory due to the interaction between thermal buoyancy force and electrical body force. The thermal boundary layer is perturbed by the electric field when it extends over the recirculation region. It can be concluded that for low Rayleigh number, the flow and temperature fields have been substantially affected by the electric field. However, the effect of EHD is diminished at high Rayleigh number which can be indicated that no significantly change in the heat transfer enhancement.

Fig. 5.58 conducts the flow and temperature fields with the multiple fins attached while the electrodes are placing at the top (x = 1.875 cm), extreme (x = 4.6875 cm), top-extreme (x = 4.6875 cm), and middle (x = 7.5 cm) arrangements, in which the numbers of fins and electrodes are remained at seven (V_0 = 12.0 kV, Ra = 10^6, N = 7, θ = 90°, AR = 0.5, and AH = 0.5). It can be observed that the top arrangement positioned yields the multiple vortices which reduces the flow structure, while the extreme arrangement performs the maximum volume flow rate from the high velocity along the hot wall compared with other arrangements. Fig. 5.59 presents the effect of inclination to the flow pattern and temperature distribution in the open cavities of θ = 0°, 30°, 60°, and 120° that has the top electrode arrangement (V_0 = 12.0 kV, Ra = 10^6, N = 7, AR = 0.5, and AH = 0.5). The case for θ = 0° in Fig. 5.59(a) corresponds that a convective regime is developed and the convection strength has strongest at θ = 60° in Fig. 5.59(b). In contrast, when the inclined angle increases further, especially at 120° (Fig. 5.59(d)), the circulation strength is considerably reduced and a non-symmetrical cells occur as same as at θ = 60°. This is expected since the cold fluid enters the cavities added by the gravity and the hot fluid exits almost horizontally. It can be seen that temperature gradient along the hot wall in case of θ = 60° is highest, thus the convective heat transfer should be highest. At θ = 120°, the isotherm lines indicate quasi-conductive regime along the boundaries because the hot wall is facing downward on this case.

The average volume flow rate and heat transfer enhancements over the period of periodic state or over the entire time span of non-periodic state (evaluated using the ratio of the average Nusselt number in the presence of an electric field to that without an electric field) along a cavity for various Rayleigh numbers is shown in Figs. 5.60 and 5.61 (N = 1, θ = 90°, AR = 0.5, and AH = 0.5). For non-EHD, placing a fin on the left wall always reduces the heat transfer on the left wall. The average Nusselt number for the left wall becomes smaller with the increasing of the fin length due to the fin obstructs flow and also reduces convective strength. However, the effect of fin becomes less remarkable with the rising of the Rayleigh number because the primary flow is enhanced with compensate the effect of blocking by the fin. Thus, for high Rayleigh number, the flow field is augmented regardless of the length and position of fin. Therefore, it is found that EHD augmented flow and heat transfer play much important role at the low Rayleigh number region, and this phenomenon is consequently influenced at the high supplied voltage.

In Fig. 5.62, one can see that the effect of the electrode arrangement on the multiple fins becomes more remarkable with the rising of the volume flow rate due to the fact that it has minimum thermal boundary layer thickness along the fin. Augmented distributions of the heat transfer for various inclined angles is indicated in Fig. 5.63 (V_0 = 12.0 kV, N = 7, AR = 0.5, and AH = 0.5). For varying an inclined angle from 0° to 120°, the volume flow rate in non-EHD increases rapidly with the increasing of Rayleigh number and thereafter taper on. The volume flow rate is generally higher when the hot wall facing up and lower when facing down, heat transfer coefficient follows a similar trend to that of volume flow rate. Therefore, the optimum inclined angle is appeared at θ = 60° and the worse case occurs at θ = 120° on both categories. However, when the attention is brought on to an enhanced ratio, the maximum value is found at θ=120° due to the lowest value from non-EHD phenomenon.

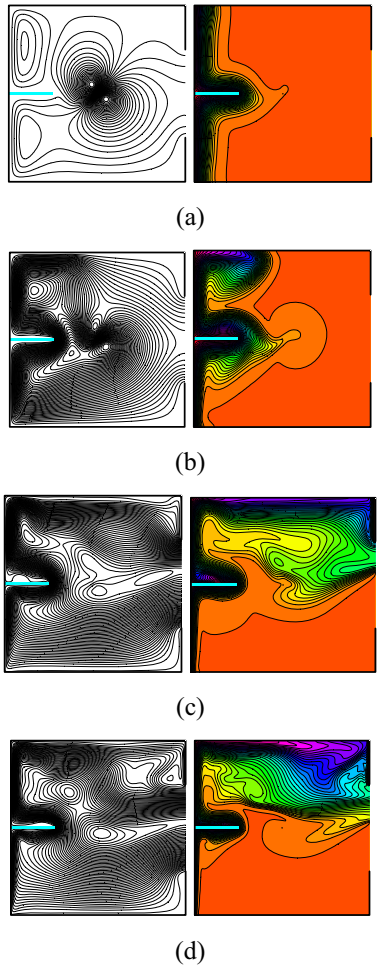

(a)

(b)

(c)

(d)

Fig. 5.57 Stream function and isotherm line contours inside the cavities for various Rayleigh numbers (V_0 = 12.0 kV, N = 1, θ = 90°, AR = 0.5, and AH = 0.5): (a) Ra = 10^4, (b) Ra = 10^5, (c) Ra = 10^6, and (d) Ra = 10^7.

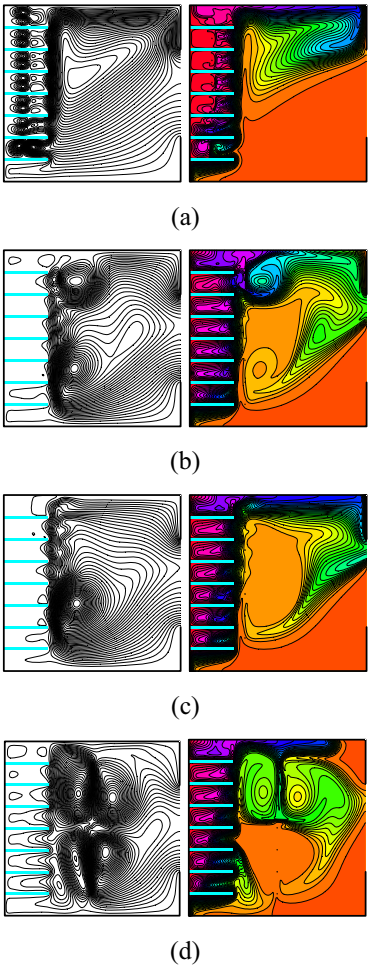

Fig. 5.58 Electrode arrangement effect on the flow and temperature fields of the multiple fins (V_0 = 12.0 kV, Ra = 10^6, N = 7, θ = 90°, AR = 0.5, and AH = 0.5): (a) top, (b) extreme, (c) top-extreme, and (d) middle.

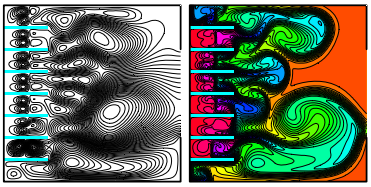

(a)

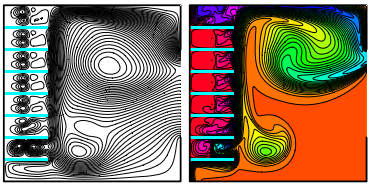

(b)

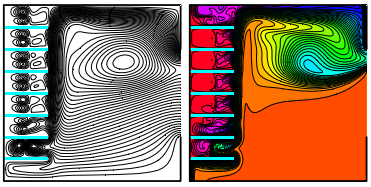

(c)

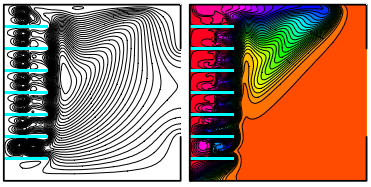

(d)

Fig. 5.59 Stream function and isotherm line contours inside the cavities for various inclined angles (V_0 = 12.0 kV, Ra = 10^6, N = 7, AR = 0.5, and AH = 0.5): (a) θ = 0°, (b) θ = 30°, (c) θ = 60°, and (d) θ = 120°.

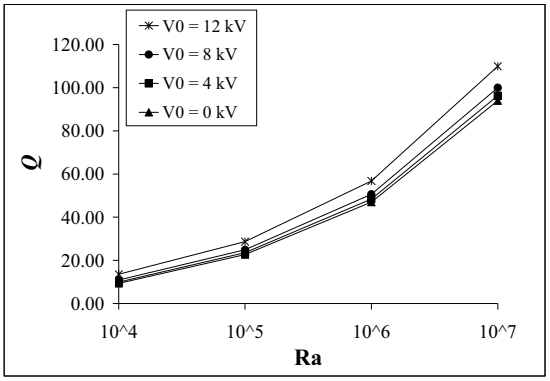

Fig. 5.60 Volume flow rate as a function of Rayleigh number ($N = 1$, $\theta = 90°$, AR = 0.5, and AH = 0.5).

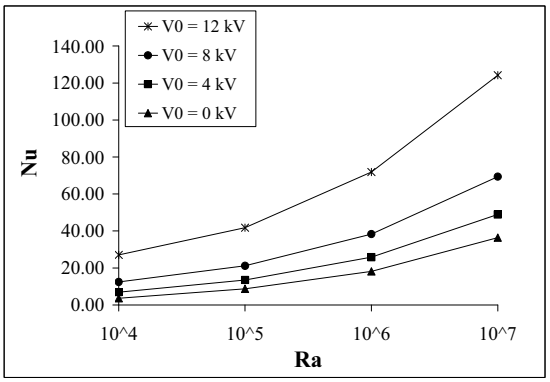

Fig. 5.61 Nusselt number as a function of Rayleigh number ($N = 1$, $\theta = 90°$, AR = 0.5, and AH = 0.5).

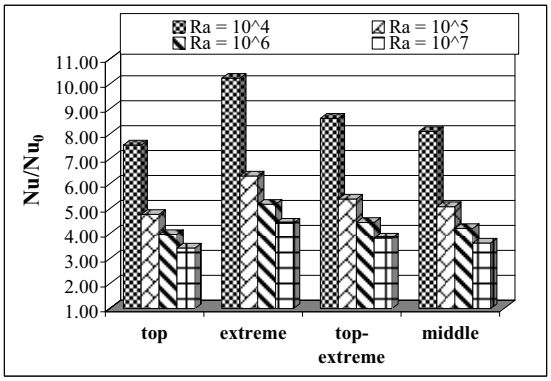

Fig. 5.62 Heat transfer enhancement for various electrode arrangements ($V_0 = 12.0$ kV, $N = 7$, $\theta = 90°$, AR = 0.5, and AH = 0.5).

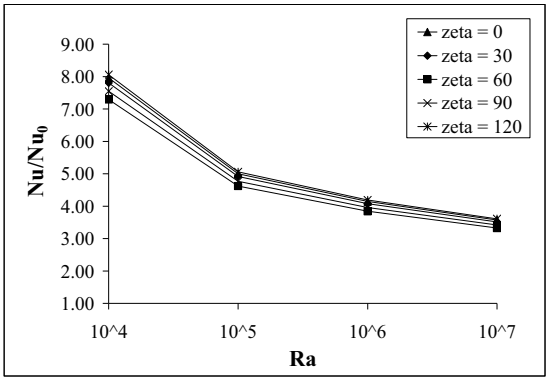

Fig. 5.63 Effect of the inclined angle on the augmented heat transfer (V_0 = 12.0 kV, N = 7, AR = 0.5, and AH = 0.5).

CHAPTER 6 CONCLUSION AND RECOMMENDATION

6.1 Conclusion

6.1.1 Flow pattern of the fluid is affected by the supplied voltage. The thermal boundary layer along the surface is perturbed by the electric field effect and also decreases at high supplied voltage.

6.1.2 The enhancement of heat transfer coefficient with the presence of an electric field increases in relation with the higher supplied voltage but decreases when the Reynolds number and Rayleigh number is augmented.

6.1.3 Channel height affects to the collector efficiency. Lower the height gives stronger strength of the electric field which results in better thermal performance.

6.1.4 The heat transfer also depends on the electrode arrangement, number of electrodes, and grounded surface geometry.

6.1.5 For open channel and open cavity, the volume flow rate enhancement reaches to a maximum at an intermediate number of electrodes and reduces furthermore when the number of electrodes is rather high due to the pressure drop effect.

6.1.6 The best augmented heat transfer for a fixed number of electrodes yields a recommended ratio of unity for the distance between wire electrodes to the distance between the grounded plates.

6.1.7 For optimum design of finned configuration, it should be considering the constraint between all concerning parameters.

6.2 Recommendation

6.2.1 From these results, placing electrodes into the appropriate arrangement with the optimum number reveals the best performance on both efficiency and economy.

6.2.2 This research can be developed for further applications to find out the optimized condition of the combination between electrohydrodynamic, extended surface, and other (such as magnetohydrodynamic) techniques of fluid flow through the extended surfaces.

CHAPTER 7 OUTPUT FROM THE RESEARCH

7.1 Kasayapanand N, Kiatsiriroat T. *Enhanced heat transfer in partially open square cavities with thin fin by using electric field.* Energy Conversion and Management (accepted).

7.2 Kasayapanand N. *A computational fluid dynamics modeling of natural convection in finned enclosure under electric field.* Applied Thermal Engineering (in press).

7.3 Kasayapanand N. *Electrohydrodynamic enhancement of heat transfer in vertical fin array using computational fluid dynamics technique*. International Communications in Heat and Mass Transfer **2008**; 35: 762-770.

7.4 Kasayapanand N. *Enhanced heat transfer in inclined solar chimneys by electrohydrodynamic technique*. Renewable Energy **2008**; 33: 444-453.

7.5 Kasayapanand N. *Numerical modeling of the effect of number of electrodes on natural convection in an EHD fluid.* Journal of Electrostatics **2007**; 65: 465-474.

7.6 Kasayapanand N. *Numerical modeling of natural convection in partially open square cavities under electric field.* International Communications in Heat and Mass Transfer **2007**; 34: 630-643.

7.7 Kasayapanand N. *Electrode arrangement effect on natural convection*. Energy Conversion and Management **2007**; 48: 1323-1330.

7.8 Kasayapanand N, Kiatsiriroat T. *Numerical modeling of the electrohydrodynamic effect to natural convection in vertical channels*. International Communications in Heat and Mass Transfer **2007**; 34: 162-175.

7.9 Kasayapanand N, Kiatsiriroat T. *Optimized mass flux ratio of double-flow solar air heater with EHD*. Energy **2007**; 32: 1343-1351.

REFERENCES

[1] Whillier A., Plastic covers for solar collectors, *Solar Energy*, **7**, 148–154, 1963.

[2] Close D.J., Solar air heaters for low and moderate temperature applications, *Solar Energy*, **7**, 117-124, 1963.

[3] Whiller A., Performance of black-painted solar air heaters of conventional design, *Solar Energy*, **8**, 31-37, 1964.

[4] Gupta C.L. and Garg H.P., Performance studies on solar air heaters, *Solar Energy*, **11**, 25-31, 1967.

[5] Tan H.M. and Charters W.W.S., Experimental investigation of forced-convective heat transfer for fully-developed turbulent flow in a rectangular duct with asymmetric heating, *Solar Energy*, **13**, 121-125, 1970.

[6] Close D.J. and Dunkle R.V., Behaviour of adsorbent energy storage beds, *Solar Energy*, **18**, 287-292, 1976.

[7] Liu C.H. and Sparrow E.M., Convective-radiative interaction a parallel plate channel-application to air-operated solar collectors, *Int. J. Heat Mass Transfer*, **23**, 1137-1146, 1980.

[8] Parkar B.F., Derivatavation of efficiency and loss factors for solar air heaters, *Solar Energy*, **26**, 27-32, 1981.

[9] Yeh H.M. and Ting Y.C., Effects of free convection on collector efficiencies of solar air heaters, *Appl. Energy*, **22**, 145-155, 1986.

[10] Satcunanathan S. and Deonarine S.A., Two-pass solar air heater, *Solar Energy*, **15**, 41-49, 1973.

[11] Wijeysundera N.E., Ah L.L., and Tjioe L.E., Thermal performance study of two-pass solar air heaters, *Solar Energy*, **28**, 363-370, 1982.

[12] Garg H.P., Sharma V.K., and Bhargava A.K., Theory of multiple-pass solar air heaters, *Energy*; **10**, 589-599, 1985.

[13] Metais B. and Eckert E.R.G., Force, free, and mixed convection regimes, *J. Heat Transfer*, **86**, 295-296, 1964.

[14] Mori Y. and Uchida Y., Forced convection heat transfer between horizontal flat plates, *Int. J. Heat Mass Transfer*, **9**, 803-817, 1966.

[15] Cheng K.C., Hong S.W. and Hwang G.J., Buoyancy effects on laminar heat transfer in the thermal entrance region of horizontal rectangular channels with uniform wall heat flux of large Prandtl number fluid, *Int. J. Heat Mass Transfer*, **15**, 1819-1836, 1972.

[16] Incropera F.P., Knox A.J., and Maughan J.R., Mixed convection flow and heat transfer in the entry region of a horizontal rectangular duct, *J. Heat Transfer*, **109**, 434-439, 1987.

[17] Maughan J.R. and Incropera F.P., Mixed convection heat transfer for airflow in a horizontal and inclined channel, *Int. J. Heat Mass Transfer*, **30**, 1307-1318, 1987.

[18] Osborne D.G. and Incropera F.P., Laminar mixed convection heat transfer for flow between horizontal parallel plates with asymmetric heating, *Int. J. Heat Mass Transfer*, **28**, 207-217, 1985.

[19] Osborne D.G. and Incropera F.P., Experimental study of mixed convection heat transfer for transitional and turbulent flow between horizontal, parallel plates, *Int. J. Heat Mass Transfer*, **28**, 1337-1344, 1985.

[20] Lund K.O., General thermal analysis of parallel-flow flat-plate solar collector absorbers, *Solar Energy*, **5**, 443-450, 1986.

[21] Yabe A., Mori Y., and Hijikata K., EHD Study of the corona wind between wire and plate electrodes, *AIAA J.*, **16**, 340-345, 1978.

[22] Velkoff H.R. and Godfrey R., Low velocity heat transfer to a flat plate in the presence of a corona discharge in air, *J. Heat Transfer*, **101**, 157-163, 1979.

[23] Yamamoto T. and Velkoff H.R., Electrohydrodynamics in an electrostatic precipitator, *J. Fluid Mech*, **108**, 1-18, 1981.

[24] Franke M.E. and Hogue L.E., Electrostatic cooling of a horizontal tube, *J. Heat Transfer*, **113**, 544-548, 1991.

[25] Kikuchi K., Taketani T., and Yabe A., Electroconvection in heat pipe application, *Preprints of the 6th International Heat Pipe Conference*, Begell House, U.S.A., **1**, 563-567, 1987.

[26] Lean M.H. and Domoto G.A., Charge transport in Navier-Strokes flow, *IEEE Transactions on Magnetics*, **24**, 262-265, 1988.

[27] McDonald J.R., Smith W.B., Spencer III H.W., and Sparks L.E., A mathematical model for calculating electrical conditions in wire duct electrostatic precipitation devices, *J. Appl. Phys.*, **48**, 2231-2243, 1977.

[28] Lawless P.A. and Sparks L.E., A mathematical model for calculating effects of back corona in wire-duct electrostatic precipitators, *J. Appl. Phys.*, **51**, 242-256, 1980.

[29] Kallio G.A. and Stock D.E., Computation of electrical conditions inside wire-duct electrostatic precipitators using a combined finite-element, finite difference technique, *J. Appl. Phys.*, **59**, 999-1005, 1985.

[30] Yabe A., Active heat transfer enhancement by apply electric field, *ASME-JSME Thermal Engineering Joint Conference*, **3**, xv-xxiii, 1991.

[31] Ishiguro H., Nagata S., Yabe A., and Nariai H., Augmentation of forced-convection heat transfer by applying electric fields to disturb flow near a wall, *ASME-JSME Thermal Engineering Joint Conference*, **3**, 25-31, 1991.

[32] Cooper P., Practical design aspects of EHD heat transfer enhancement in evaporator, *ASHRAE Transactions*, **98**, 445-454, 1992.

[33] Ogata J., Iwafuji Y., Shimada Y., and Yamazaki T., Boiling heat transfer enhancement in tube-bundle evaporators utilizing electric field effects, *ASHRAE Transactions*, **98**, 435-444, 1992.

[34] Yeh H.M. and Lin T.T., The effect of collector aspect ratio on the collector efficiency of flat-plate solar air heaters, *Energy*, **20**, 1041-1047, 1995.

[35] Allen P.H.G. and Karayiannis T.G., Review paper electrohydrodynamic enhancement of heat transfer and fluid flow, *Heat Recovery Systems & CHP*, **15**, 389-423, 1995.

[36] Singh A., Ohadi M.M., and Dessiatoun S., EHD enhancement of in-tube condensation heat transfer of alternate refrigerant R-134a in smooth and microfin tubes, *ASHRAE Transactions*, **103**, 813-823, 1997.

[37] Hachemi A., Thermal heat performance enhancement by interaction between the radiation and convection in solar air heaters, *Renewable Energy,* **12**, 419-433, 1997.

[38] Karayiannis T.G., EHD boiling heat transfer enhancement of R123 and R11 on a tube bundle, *Applied Thermal Engineering*, **18**, 809-817, 1998.

[39] Yeh H.M., Ho C.D., and Hou J.Z., The improvement of collector efficiency in solar air heaters by simultaneously air flow over and under the absorbing plate, *Energy*, **24**, 857–871, 1999.

[40] Pottler K., Sippel C.M., Beck A., and Fricke J., Optimized finned absorber geometries for solar air heating collectors, *Solar Energy*, **67**, 35–52, 1999.

[41] Jiracheewanun S., Tiansuwan J., and Kiatsiriroat T., Heat transfer characteristics of fluid flow through a tube bank under electric field, *14TH National Mechanical Engineering Conference*, Thailand, 80-86, 2000.

[42] Verma S.K. and Prasad B.N., Investigation for the optimal thermohydraulic performance of artificially roughness solar air heaters, *Renewable Energy*, **20**, 19-36, 2000.

[43] Wangnippanto S., Tiansuwan J., Jiracheewanun S., Wang C.C., and Kiatsiriroat T., Air side performance of thermosyphon heat exchanger in low Reynolds number region: with and without electric field, *Int. J. Energy Conversion and Management*, **43**, 1791-1800, 2002.

[44] Yeh H.M., Ho C.D., and Hou J.Z., Collector efficiency of double-flow solar air heaters with fins attached, *Energy*, **27**, 715–727, 2002.

[45] Momin A.M.E., Saini J.S., and Solanki S.C., Heat transfer and friction in solar air heater duct with V-shaped rib roughness on absorber plate, *Int. J. Heat Mass Transfer*, **45**, 3383–3396, 2002.

[46] Bhagoria J.L., Saini J.S., and Solanki S.C., Heat transfer coefficient and friction factor correlations for rectangular solar air heater duct having transverse wedge shaped rib roughness on the absorber plate, *Renewable Energy*, **25**, 341-369, 2002.

[47] Mathew J. and Lai F.C., Enhanced heat transfer in a horizontal channel with double electrodes, *Conference Record of the 1995 IEEE*, 1472-1479, 1995.

[48] Yadav Y.P., Kumar A., Sharan L.B., and Srivastava V.P., Parametric analysis of a suspended flat plate solar air heater, *Int. J. Energy Conversion and Management*, **36**, 325-335, 1995.

[49] Goo J.H. and Lee J.W., Stochastic simulation of particle charging and collection characteristics for a wire-plate electrostatic precipitator of short length, *J. Aerosol Sci.*, **28**, 875-893, 1997.

[50] Tada Y., Takimoto A., and Hayashi Y., Heat transfer enhancement in a convective field by applying ionic wind, *J. Enhance Heat Transfer*, **4**, 71-88, 1997.

[51] Yang H. and Lai F.C., Effects of Joule heating on EHD-enhanced natural convection in an enclosure, *IEEE Industry Applications Society Annual Meeting*, **3**, 1851-1858, 1997.

[52] Badr H. and Kocabiyik M.S., Symmetrically oscillating viscous flow over an elliptic cylinder, *J. Fluid and Structures*, **11**, 745-766, 1997.

[53] Lami E., Mattachini F., Sala R., and Vigl H., A mathematical model of electrostatic field in wires-plate electrostatic precipitators, *J. Electrostat.*, **39**, 1-21, 1997.

[54] Choi B.S. and Fletcher C.A.J., Turbulent particle dispersion in an electrostatic precipitator, *Applied Mathematical Modelling*, **22**, 1009-1021, 1998.

[55] Peek F.W., *Dielectric phenomena in high voltage engineering*, McGraw-Hill, New York, 1929.

[56] Rafiroiu D., Suarasan I., Morar R., Atten P., and Dascalescu L., Inception of corona discharges in typical electrode configurations for electrostatic processes applications, *IEEE Industry Applications Society Annual Meeting*, **1**, 387-392, 1999.

[57] Arulanandam S.J., Hollands K.G.T., and Brundrett E., A CFD heat transfer analysis of the transpired solar collector under no-wind conditions, *Solar Energy*, **67**, 93-100, 1999.

[58] Hegazy A.A., Optimum channel geometry for solar air heaters of conventional design and constant flow operation, *Int. J. Energy Conversion and Management*, **40**, 757-774, 1999.

[59] Demirel Y., Al-Ali H.H., and Abu-Al-Saud B.A., Enhancement of convection heat-transfer in a rectangular duct, *Applied Energy*, **64**, 441-451, 1999.

[60] Hilmer F., Vajen K., and Ratka A., Ackermann H., Fuhs W., and Melsheimer O., Numerical solution and validation of a model of solar collector working with varying fluid flow rate, *Solar Energy*, **65**, 305–321, 1999.

[61] Gao W., Lin W., and Lu E., Numerical study on natural convection inside the channel between the flat-plate cover and sine-wave absorber of a cross-corrugated solar air heater, *Int. J. Energy Conversion and Management*, **41**, 145-151, 2000.

[62] Talaie M.R., Taheri M., and Fathikaljahi J., A new method to evaluate the voltage-current characteristics applicable for a single-stage electrostatic precipitator, *J. Electrostat.*, **53**, 221-233, 2001.

[63] Rafiroiu D., Munteanu C., Morar R., Meroth A., Atten P., and Dascalescu L., Computation of the electric field in wire electrode arrangements for electrostatic processes application, *J. Electrostat.*, **52**, 571-577, 2001.

[64] Ozsunar A., Baskaya S., and Sivrioglu M., Numerical analysis of Grashof number, Reynolds number and inclination effects on mixed convection heat transfer in rectangular channels, *Int. Comm. Heat Mass Transfer,* 28, 985-994, 2001.

[65] Anagnostopoulos J. and Bergeles G., Corona discharge simulation in wire-duct electrostatic precipitator, *J. Electrostat.*, **54**, 129-147, 2002.

[66] Gunnewiek L.H., Hollands K.G.T., and Brundrett E., Effect of wind on flow distribution in unglazed transpiredplate collectors, *Solar Energy*, **72**, 317-325, 2002.

[67] Kazeminejad H., Numerical analysis of two dimensional parallel flow flat-plate solar collector, *Renewable Energy*, **26**, 309-323, 2002.

[68] Kasayapanand N., Tiansuwan J., Asvapoositkul W., Vorayos N., and Kiatsiriroat T., Effect of the electrode arrangements in tube bank on the characteristic of electrohydrodynamic heat transfer enhancement: low reynolds number, *J. Enhanced Heat Transfer*, **9**, 229-242, 2002.

[69] Ammari H.D., A mathematical model of thermal performance of a solar air heater with slats, *Renewable Energy*, **28**, 1597-1615, 2003.

[70] Abu-Hamdeh N.H., Simulation study of solar air heater, *Solar Energy*, **74**, 309-317, 2003.

APPENDIX A

PUBLICATIONS

A-1 Kasayapanand N, Kiatsiriroat T. *Enhanced heat transfer in partially open square cavities with thin fin by using electric field.* Energy Conversion and Management (accepted).

A-2 Kasayapanand N. *A computational fluid dynamics modeling of natural convection in finned enclosure under electric field.* Applied Thermal Engineering (in press).

A-3 Kasayapanand N. *Electrohydrodynamic enhancement of heat transfer in vertical fin array using computational fluid dynamics technique*. International Communications in Heat and Mass Transfer **2008**; 35: 762-770.

A-4 Kasayapanand N. *Enhanced heat transfer in inclined solar chimneys by electrohydrodynamic technique*. Renewable Energy **2008**; 33: 444-453.

A-5 Kasayapanand N. *Numerical modeling of the effect of number of electrodes on natural convection in an EHD fluid*. Journal of Electrostatics **2007**; 65: 465-474.

A-6 Kasayapanand N. *Numerical modeling of natural convection in partially open square cavities under electric field.* International Communications in Heat and Mass Transfer **2007**; 34: 630-643.

A-7 Kasayapanand N. *Electrode arrangement effect on natural convection*. Energy Conversion and Management **2007**; 48: 1323-1330.

A-8 Kasayapanand N, Kiatsiriroat T. *Numerical modeling of the electrohydrodynamic effect to natural convection in vertical channels*. International Communications in Heat and Mass Transfer **2007**; 34: 162-175.

A-9 Kasayapanand N, Kiatsiriroat T. *Optimized mass flux ratio of double-flow solar air heater with EHD*. Energy **2007**; 32: 1343-1351.